

## Probing Temperature and Degree-of-conversion States via Tomographic Fluorescence Imaging

Sui Man Luk<sup>a,b,†</sup>, Chi Chung Li<sup>b,†</sup>, Joseph Toombs<sup>b</sup>, Martin de Beer<sup>c</sup>, Hayden Taylor<sup>b</sup>

<sup>a</sup>Biophysics Graduate Group, University of California, Berkeley, Berkeley, CA 94720, USA

<sup>b</sup>Department of Mechanical Engineering, University of California, Berkeley,  
Berkeley, CA 94720, USA

<sup>c</sup>Lawrence Livermore National Laboratory, Livermore, CA, USA 94550

†These authors contributed equally to this work.

### Abstract

Tomographic volumetric additive manufacturing rapidly solidifies freeform objects via photopolymerization, which raises both local temperature and degree-of-conversion (DOC). In-situ monitoring of temperature and DOC during the printing process is crucial for metrology and process control. In this study, we propose a tomographic fluorescence imaging technique to detect the spatiotemporal evolution of temperature and DOC during volumetric printing. Our solution employs a fluorescent dye that is sensitive to both variations in temperature and DOC. DOC is considered as a function of, and is expressed in, the absorbed optical dose of the resin. By tomographically measuring changes in the dye's fluorescence intensity and feeding such changes to a temperature–dose–intensity calibration, the local dose and temperature during the print can be confined to a set of possible states. At exemplar locations where *a priori* information is known for one quantity, the other quantity can be resolved. This work illustrates the potential of and lays foundations for the development of two-wavelength spatiotemporal measurement systems that uniquely resolve both temperature and DOC.

### Introduction

From point-scanning to plane-scanning and volume-at-once methods, advancements in parallelization of additive manufacturing (AM) have reduced the processing time by orders of magnitude. While parallelization has dramatically improved the practicality of these AM methods, the challenge of heat generation has become increasingly critical. Vat AM techniques such as continuous liquid interface production [1], [2], xolography [3], and computed axial lithography (CAL) [4] all exothermically solidify a large volume of photoresins in the order of minutes. For volumetric AM (VAM) such as CAL, the generated heat can auto-accelerate the polymerization reaction, trigger convection flows which lead to part floating [5]–[7], and cause optical aberrations. Due to the strong influence of temperature on reaction rates, rheological behavior, and thermal lensing effects, temperature measurement alongside conversion state monitoring is crucial for devising mitigation strategies and implementing process control.

Although heat generation have been acknowledged as one of the fabrication speed limiters in layer-based AM [2], the equivalent thermal challenges in VAM are not yet studied due to the lack of a volumetric thermal monitoring method. Infrared (IR) thermometry cannot be easily applied in volumetric measurements as it faces challenges such as limited transmission, material-dependent absorption peaks, and high background signals emitted by other objects. Thermal imaging using visible light from blackbody radiation, as used in reactive sintering [8], is not applicable to VAM due to much lower reaction temperature.

Currently, methods for in-situ monitoring in volumetric AM are primarily focused on degree of conversion (DOC) rather than temperature. Color schlieren tomography (CST) [9], [10] is designed to reconstruct local refractive index changes and quantify local material conversion through conversion–index relationships. On the other hand, optical scattering tomography (OST) [11], [12] infers material conversion from reconstructed scattering density. While both spatiotemporally resolved techniques have the potential to provide process control feedback from a conversion perspective, their current development has not addressed the exothermic nature of the process.

Fluorescence thermometry, also known as luminescence molecular thermometry, offers a viable alternative. This technique has been successfully employed to monitor temperatures in small-scale and biological environments [13]. It provides a variety of readouts including fluorescence intensity, fluorescence lifetime, and absorption/emission spectrum, offering resolution down to sub-degree Celsius. Yet, these measurements are commonly made in 2D. Although 3D measurements have been made with confocal microscopy, tomographic measurements, which enable larger (cm-scale) isotropic measurements, have not been performed.

In this work, we exploit the dependence of Rhodamine B (RhB) on the surrounding temperature and DOC to infer their possible values during a print. RhB is a cost-effective, widely available, and well-studied fluorophore. It is highly soluble in the resins used in this study at the concerned concentration (5  $\mu\text{M}$ ). RhB's sensitivity to viscosity and temperature of the environment has been demonstrated previously [14]–[16]. Here, we employ tomographic fluorescence imaging to measure spatiotemporally the intensity of these luminescent molecular thermometers, providing a relationship between temperature and DOC (expressed in terms of absorbed dose) at various points in space and time. With *a priori* information on one of the quantities, this relationship allows us to determine the other unknown quantity. For materials undergoing significantly exothermic reactions, our method can discern the geometry of the printed object before material conversion develops to a stage where it begins to scatter light appreciably. The method can also quantify the temperature change in the surrounding uncured region.

## Methodology

### *Resin formulation*

To demonstrate the system's capability to detect thermal change in the print, a polymer precursor is chosen such that a significant amount of heat is generated over the course of tomographic VAM printing with a typical patterning light intensity. Pentaerythritol Tetraacrylate (CAS no. 4986-89-4, TCI) (PETRA) with 0.1 wt% Irgacure-369 (CAS no. 119313-12-1, Sigma-Aldrich) (I369) was found to release substantial heat under typical VAM patterning light intensity ( $8 \text{ mW/cm}^2$ ) over the course of 1–2 minutes, making the resin a good candidate for rapid testing of our detection system. Poly (ethylene glycol) diacrylate (average molecular weight 700) (CAS no. 26570-48-9, Sigma Aldrich) (PEGDA-700) with 0.3 mM Phenylbis(2,4,6-trimethylbenzoyl) phosphine oxide (CAS no.162881-26-7, Sigma Aldrich) (BAPO) was also prepared for separate material characterization. The concentration of RhB (CAS no. 81-88-9, Sigma Aldrich) dissolved in the resin is chosen to be  $5 \text{ }\mu\text{M}$  to provide sufficient fluorescence signal without significant attenuation of excitation light or reabsorption of emitted light within the resin volume.

### *Absorbance/emission measurement and fluorescence calibration*

The absorbance and emission spectra of resins were collected by a SpectroVis Plus UV-VIS spectrophotometer (Vernier, USA) with a custom excitation light source at 532 nm. The fluorescence of RhB in PETRA resin as a function of absorbed optical dose and temperature was collected with a SpectraMax M5 multimode microplate reader (Molecular Devices, USA). The absorbed optical dose refers to the optical dose absorbed by the photoinitiator (I369 or BAPO). This quantity has unit of  $\text{mJ/cm}^3$  and it is calculated by multiplying the areal optical dose in  $\text{mJ/cm}^2$  with the absorption coefficient of the photoinitiator at the patterning wavelength (405 nm). Resin samples across optical dose 0–93  $\text{mJ/cm}^3$  were first cured in groups of four replicates on a clear-bottom 96-well-plate (CellVis P96-1.5H-N). The plate was then read on the SpectraMax M5 microplate reader in fluorescence end-point mode with excitation wavelength = 532 nm and emission wavelength = 580 nm. A cutoff wavelength of 570 nm was set by the plate reader to filter unwanted signal from excitation light. To account for signal variation across the well area induced by uneven curing or excitation illumination, a  $3 \times 3$  point scan was done across each well and the median of the nine point signals was chosen to represent the fluorescence intensity measured at that well.

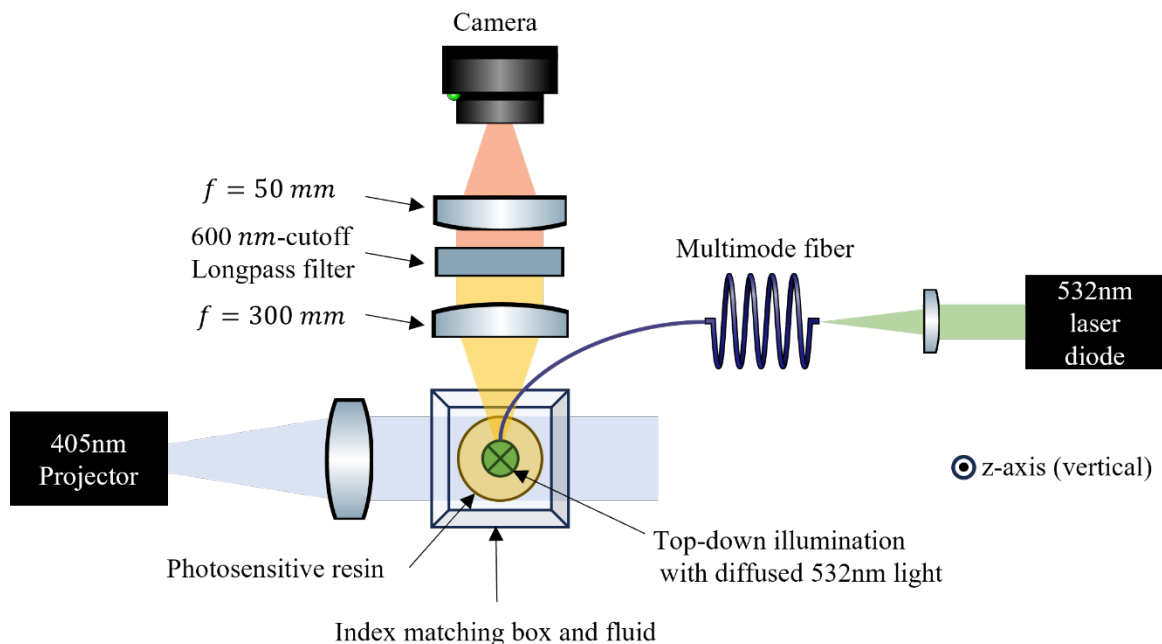


Figure 1. Schematic of tomographic fluorescence imaging system presented in this work.

### Tomographic fluorescence imaging setup

Experimental hardware for the printing and fluorescence imaging experiments is shown in Figure 1. The optical projections used for printing had a center wavelength of 405 nm and maximum intensity of 8 mW/cm<sup>2</sup> and were discretized at a spatial sampling rate of 32.8 pixel/mm at the sample volume. The vial containing the resin was immersed in a mineral oil index matching bath and was rotated at 30 °/s during the experiment. A multimode optical fiber (Thorlabs AFS105/125Y) carried the excitation light output from a 532 nm diode laser to the fiber port mounted on the top of the hollow shaft rotation stage. From the optical fiber, the 532 nm light illuminated the resin from above and through a diffuser.

The sample fluorescence was collected and imaged by a 4f system comprising two lenses with focal length of 300 mm and 50 mm (Thorlabs AC508-300-A-ML and LA1131-ML), through a long-pass filter (Thorlabs FELH0600) to a monochrome camera (Thorlabs 340M-USB). At the resulting 6× demagnification, the camera effectively sampled the fluorescent resin at 22.5 pixel/mm.

Image acquisition was electronically triggered to synchronize with the intermittent off-time of the patterning projection. Effectively, this synchronization prevented the camera from capturing the non-uniform fluorescence caused by the 405 nm patterning beam. Details of this electronic synchronization are described in the supplementary materials S.1.

### *Computational reconstruction*

A multi-processing Python program was written to control the projector, diode laser and camera. The data acquisition and processing pipeline is detailed in supplementary materials S.2. During printing, a sequence of pre-computed patterning images was delivered by the projector to the resin. The set of images spanned a full vial rotation and contained one projected image per degree of rotation. These projections were optimized for the test object with the OSMO algorithm [17].

To estimate the spatial distribution of the resulting fluorescence intensity within the resin, the collected camera images were first denoised with a Gaussian filter and then used for reconstruction via filtered backprojection. This digital reconstruction process is detailed in supplementary section S.2. The resulting reconstruction is a volumetric representation of the local fluorescence intensity ratio relative to the local intensity at the baseline (25 °C and 0 mJ/cm<sup>3</sup> optical dose). Over the course of an experiment, a temporal sequence of reconstructions can be produced, where each reconstruction is computed from images taken over one rotation period. Similar to CST [9], the multi-processing program is written such that reconstruction can be computed either in real-time during the experiment (at slower reconstruction refresh rates) or afterwards (at higher refresh rates). The reconstruction demonstrated in this work was computed in real-time while analyses were performed after the experiment.

## **Results**

### *Temperature- and curing-dependent optical properties of RhB*

The absorption spectrum of RhB in PETRA did not significantly overlap with that of I369 or the patterning light used in this work, which had a center wavelength of 405 nm (Figure 2). Nevertheless, the residual light absorption at approximately 405 nm by RhB necessitated the application of time-gated and synchronized projection and image acquisition (supplementary material S.1). This ensured that the camera did not capture the non-uniform fluorescence created by the patterning beam.

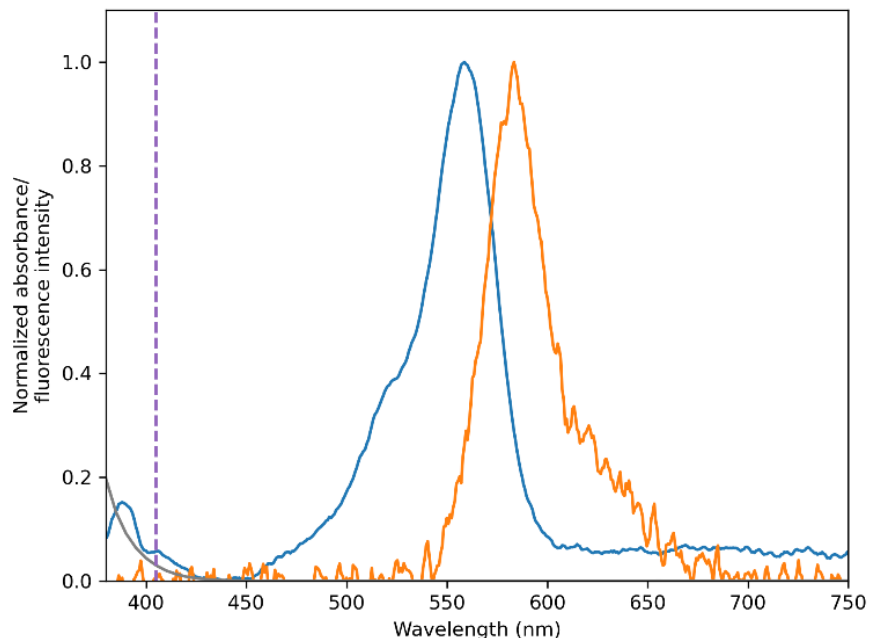


Figure 2. Normalized absorption (blue) and normalized fluorescence intensity (orange) of PETRA + 5  $\mu$ M RhB upon excitation at 532 nm and normalized absorption of 2 mM I369 in isopropanol (gray). The 405 nm patterning light used in this study is denoted by a dashed line.

As shown in Figure 3, the fluorescence of RhB excited by 532 nm decreases with temperature and absorbed optical dose of PETRA resin. In the case of unexposed resin, the fluorescence intensity drops 34 % over temperature increases of 34 °C. This corresponds to an average thermal sensitivity of 1 % per degree Celsius. Both the fluorescence intensity and its sensitivity with temperature decrease with absorbed dose. This effect can be attributed to the increased restriction of RhB molecules in the formed polymer network.

Notably, RhB's fluorescence intensity in PETRA resin declines significantly as a function of the resin's absorbed dose. A potential explanation for this could be the ionic nature of RhB versus the lower polarity of PETRA, given its tetrahedral acrylate moieties. This polarity difference could induce RhB aggregation and consequently result in fluorescence quenching [18].

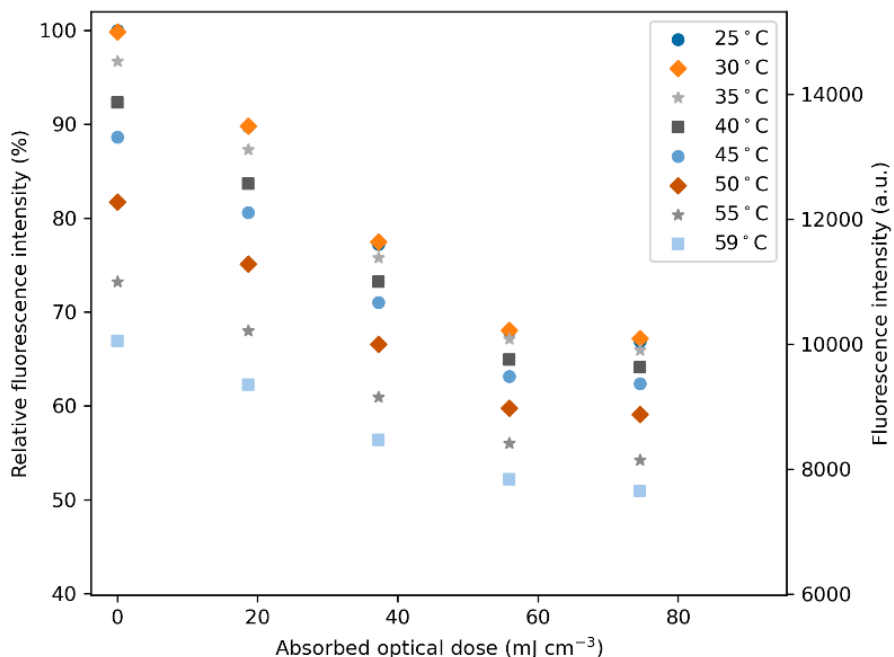


Figure 3. Fluorescence intensity (right axis) and relative fluorescence intensity compared to a baseline of 25 °C and 0 mJ/cm<sup>3</sup> absorbed dose (left axis) of PETRA + 5 μM RhB + 0.1 wt. % I369, as a function of temperature and absorbed optical dose. The polymer precursor is excited at 532 nm.

On the other hand, we also characterized the response surface of RhB in PEGDA (at the same concentration of 5 μM), which exhibited opposite trend of fluorescence with absorbed dose (Figure S2). PEGDA has a higher polarity than PETRA, which may facilitate the dispersion of RhB and allow the other temperature/exposure-dependent mechanism to dominate, such as the sensitivity related to the rotation of diethylamine groups in the molecule upon excitation as summarized in [19], [20]. These reports suggest elevated local viscosity is associated with the non-radiative decay of excited electrons, resulting in decreased fluorescence, while an increase in temperature has an opposite effect. This is in line with our intensity characterization data in Figure S2.

The formation of an amorphous polymer network induces spatial variation of refractive index and leads to scattering of both excitation light and emission from fluorophores within the material volume. As scattering lowers detected intensity in addition to temperature and exposure effects, the onset of scattering thereby established a cut-off for the absorbed dose range examined in the response surface characterization. In the above characterization, this scattering onset is indicated by an increase in measured absorbance on a well-plate following an absorbed dose of 74.6 mJ/cm<sup>3</sup> (Figure S3).

With the above material considerations in mind, we sought to detect two VAM-printed objects — a trihelix and a pyramid truss — from their changes in fluorescence intensity. The objects were printed in the PETRA resin and their fluorescence images were collected, processed, then used for tomographic reconstruction. From the raw fluorescence images (Figure 4), we can detect reduced intensity near the object. In the reconstruction (Figure 5, Figure 6), we can recover the volumetric distribution of relative fluorescence intensity ( $I_{relative}$ ) at each query

time. From the resulting reconstructions, the reduction of  $I_{relative}$  distributed in a similar shape as the printing object but extends further beyond the design part surface. The change of  $I_{relative}$  is non-uniform, indicating potentially different rates of conversion and heat diffusion. From the reconstruction in the printing of the pyramid truss (Figure 6), the largest decrease of  $I_{relative}$  happens in the five tips of the pyramid where the members of the truss meet. For an example location above the trihelix object, we extract the time series of  $I_{relative}$  and resolve its local temperature under the assumption that this location has zero absorbed optical dose as it is located outside the part and above the height range under patterning exposure. As shown on Figure 7, the temporal temperature profile computed from locally averaged  $I_{relative}$  shows a clear increase after the end of patterning at 60 s. The onset of scattering in the prints were quantified separately with dark-field imaging (supplementary section S.3) and only the results generated prior to that time point are presented in Figure 3, Figure 5, Figure 6. A separate run of the experiment was performed without printing to detect photobleaching of RhB by 532 nm excitation light. The effect of photobleaching was negligible over the course of printing up to 450 s.

There is substantial room for improvement in the signal-to-noise ratio (SNR) on the acquired image and the computed reconstructions. The high noise level in the results can be attributed to limited light collection during the short exposure time (9 ms) and with the low numerical aperture (0.085) imaging system. In future experiments SNR can be improved by using a laser with higher power and more concentrated fluorophore in resin. Temporal averaging over consecutively collected images can also be used to reduce noise.

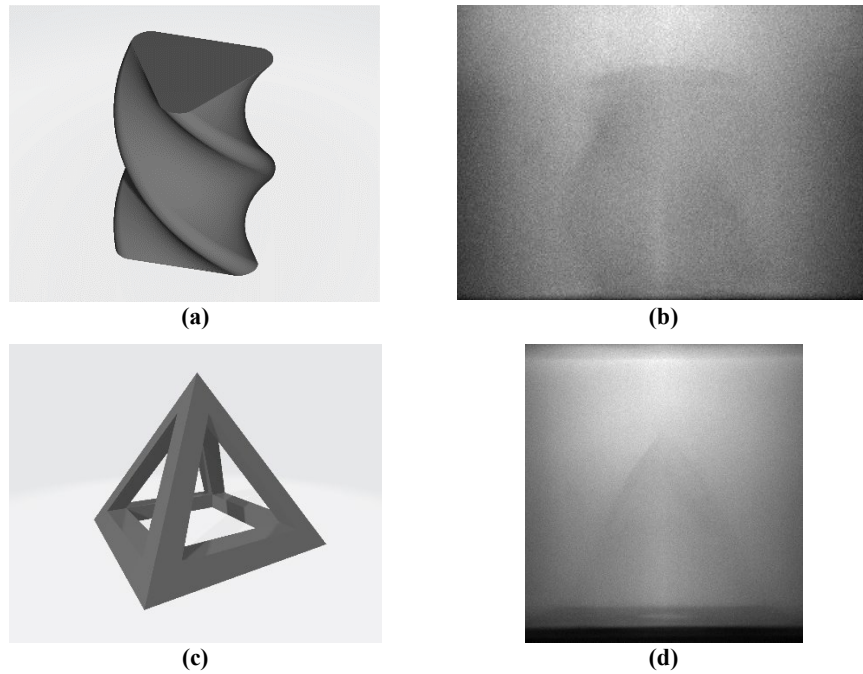


Figure 4. a) Geometry of trihelix target object, b) Raw fluorescence image captured at 166 s into printing of a trihelix, c) Geometry of pyramid truss target object, d) Raw image captured at 133 s into printing of a pyramid truss (black region at the bottom: bottom of the vial, grey region directly above: reduced fluorescence at the bottom of the pyramid truss).

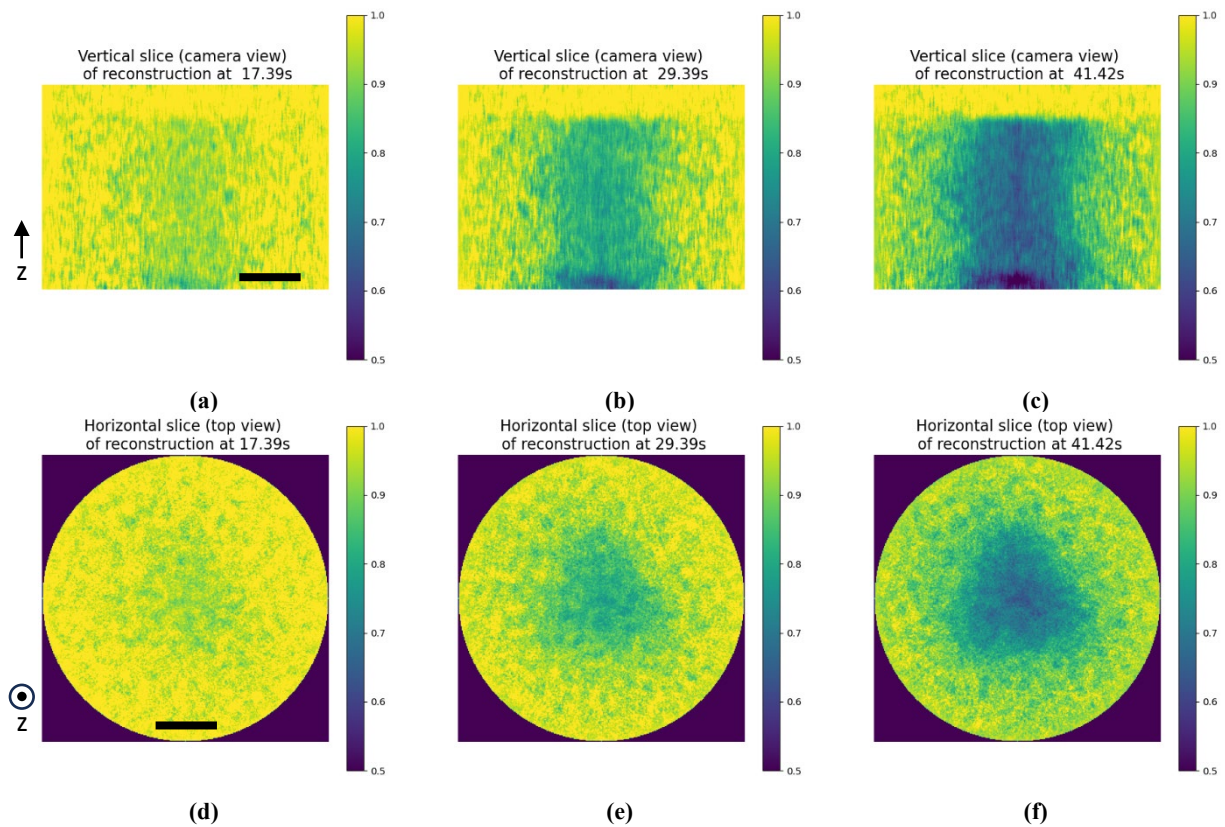


Figure 5. Central vertical (a-c) and horizontal (d-f) reconstruction slices of relative fluorescence intensity during printing of a trihelix target. Scale bar: 3 mm.

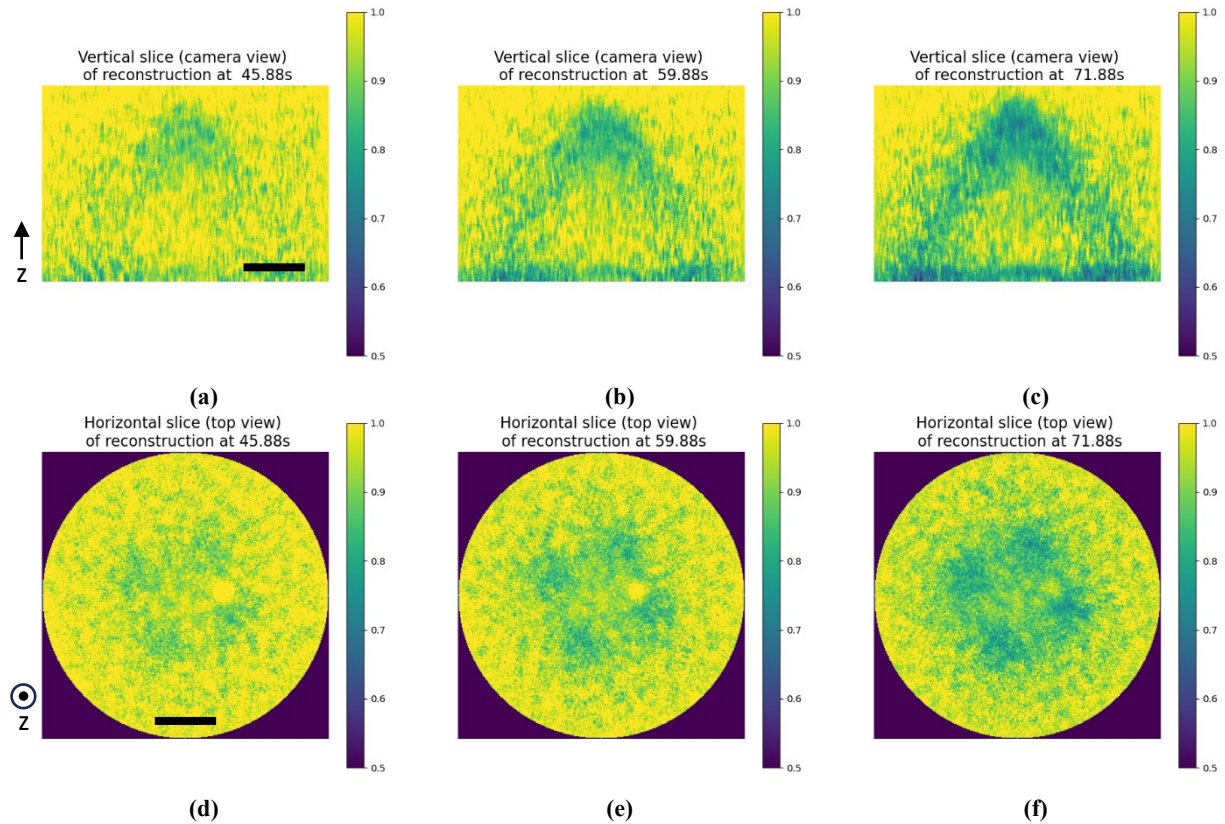


Figure 6. Central vertical (a-c) and horizontal (d-f) reconstruction slices of relative fluorescence intensity during printing of a pyramid truss target. Scale bar: 3 mm.

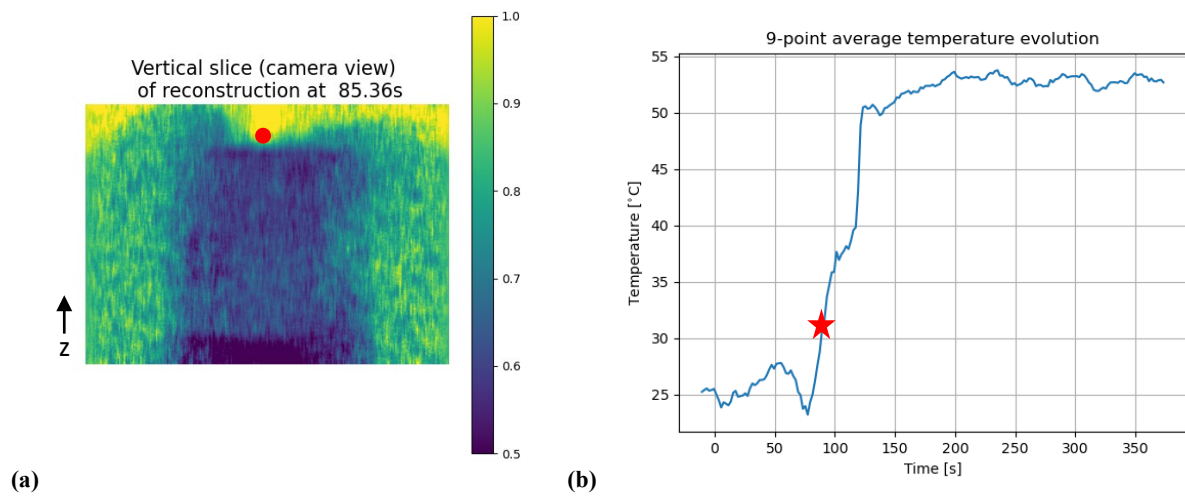


Figure 7. (a) a vertical slice of the reconstructed trihelix print at 85.36 s. (b) temporal temperature profile at a location near the top of the trihelix structure (red dot in (a)), where absorbed dose is assumed to be zero. At this location, a spatial average is taken over relative intensity in nine adjacent voxels in the horizontal plane of reconstruction. The average intensity is then mapped to temperature with the material's response surface along the line of zero absorbed dose. The red star indicates the temperature value at the location at 85.36 s.

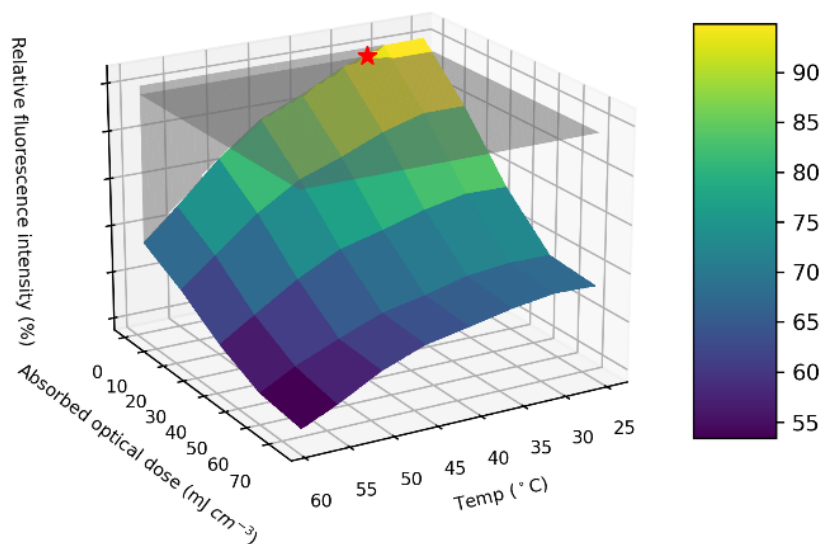


Figure 8. Illustration of obtaining material state information from RhB material response surface. Colored surface plot: response surface of PETRA + 5  $\mu\text{M}$  RhB + 0.1 wt. % I369, in terms of fluorescence intensity relative to that at 25  $^{\circ}\text{C}$  and 0  $\text{mJ}/\text{cm}^3$  absorbed dose. Intersection of a specific reconstructed relative fluorescence intensity (gray plane) and the response surface gives a set of possible corresponding temperatures and absorbed dose (gray contour line). At spatial location where the resin is unexposed (absorbed dose = 0  $\text{mJ}/\text{cm}^3$ ), the temperature at that location is uniquely determined on the response surface (red star).

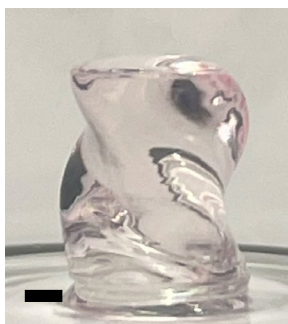


Figure 9. A printed trihelix object from captured fluorescence intensity. Scale bar: 1 mm.

## Discussion

Our research has established a tomographic fluorescence imaging system within the VAM framework for temperature and DOC characterization. The fluorescent probe implemented has demonstrated reasonable sensitivity to both temperature changes and photopolymerization exposure. Tomographic reconstruction further facilitates online and offline metrology, allowing us to capture volumetrically the evolution of temperature-dose profile both inside and outside the print, prior to the onset of substantial scattering. In a broader context, our work serves as an inaugural demonstration of tomographic measurement of material-state properties via an environment-sensitive fluorescent probe. Existing confocal measurement of state-dependent fluorescence [13] have limited axial sectioning capability at low numerical aperture (NA) due to the diffraction limit. The tomographic nature of our reconstruction method offers isotropic

voxels in a low NA regime and therefore enables volumetric measurement at cm-scale or larger. This spatiotemporally resolved material-state measurement technique also presents potential applications in other additive manufacturing modalities.

While RhB exhibited a thermal sensitivity of 1 % per degree Celsius, we also found that it demonstrated varying degrees of absorbed-dose sensitivity in different polymer precursors. RhB's thermal and absorbed-dose sensitivity is also subject to the polarity of the resin and the aggregation effect, necessitating characterization specific to each resin. In future, different fluorescent sensors can be examined for improving sensitivity. For example, BODIPY-derived molecular rotors have demonstrated tunable sensitivity to viscosity and/or temperature in both polar and non-polar solvents [19].

Certain limitations were identified in our study, particularly regarding the sensitivity of the optical system. The minimum detection level of voxel intensity change depends on the image pixel sampling rate, available bit-depth and noise level. A relation between spatial and fluorescence intensity resolution in tomographic imaging is derived in supplementary material S.4. Apart from hardware, there are various image processing decisions (such as denoising parameters) that represent tradeoffs between spatial resolution and intensity resolution. Furthermore, scattering posed a significant challenge to interpreting results generated after the onset of the phenomenon. Scattering arises from local changes in the refractive index and the self-lensing effect associated with directed patterning illumination [21]. For reconstructions after the onset of part scattering, we limited quantitative analysis to levels above the object height, as the tomographic light propagation model's accuracy was compromised by unaccounted scattering within the same height level as the object. We characterized the scattering onset of the print using a dark-field imaging setup (supplementary section S.3) and only presented results generated prior to that time point in Figure 3, Figure 5 and Figure 6. To mitigate the impact of scattering, future work could implement techniques such as tomosynthetic printing [22], [17] or latent image VAM [21], or utilize a low-shrinkage resin with a smaller change in refractive index. The dual dependence of RhB's fluorescence intensity on temperature and absorbed optical dose limits unique determination of temperature or DOC at where the other quantity is known (Figure 8). Future work could also explore dual-mode detection for simultaneous resolution of both temperature and DOC. For instance, multiple chemical probes at orthogonal wavelengths could be employed, as well as two-color ratiometric measurements on a single chemical probe.

## Conclusion

Our study established the use of RhB and tomographic fluorescence imaging for real-time monitoring of temperature and degree of conversion in volumetric additive manufacturing. The fluorescent properties of RhB demonstrated sensitivity to temperature and curing, though the exact effects varied across different polymer precursors. Scattering of light during printing limits the valid observation time and points to future investigations in conjunction with scattering-free printing methods. This study paves the way to two-wavelength spatiotemporal measurement systems that uniquely resolve both DOC and temperature.

## Acknowledgements

The authors would like to thank Dr. Sijia Huang and Dr. Maxim Shusteff for their helpful discussion on this project. We also thank Dr. Mary West of the Cell and Tissue Analysis Facility (CTAF) at UC Berkeley. This work was performed in part in the QB3 CTAF, that provided the SpectraMax M5 multimode microplate reader. We thank Dr. Paul Lum of the Biomolecular Nanotechnology Center at UC Berkeley for providing the Vernier SpectroVis Plus UV-VIS spectrophotometer. We thank Mr. Christian Castaneda for constructing a LED controller for the patterning projector. This work was funded by the National Science Foundation (NSF Award no. 2036849).

## References

- [1] J. R. Tumbleston *et al.*, “Continuous liquid interface production of 3D objects,” *Science*, vol. 347, no. 6228, pp. 1349–1352, Mar. 2015, doi: 10.1126/science.aaa2397.
- [2] D. A. Walker, J. L. Hedrick, and C. A. Mirkin, “Rapid, large-volume, thermally controlled 3D printing using a mobile liquid interface,” *Science*, vol. 366, no. 6463, pp. 360–364, Oct. 2019, doi: 10.1126/science.aax1562.
- [3] M. Regehly *et al.*, “Xolography for linear volumetric 3D printing,” *Nature*, vol. 588, no. 7839, Art. no. 7839, Dec. 2020, doi: 10.1038/s41586-020-3029-7.
- [4] B. E. Kelly, I. Bhattacharya, H. Heidari, M. Shusteff, C. M. Spadaccini, and H. K. Taylor, “Volumetric additive manufacturing via tomographic reconstruction,” *Science*, vol. 363, no. 6431, pp. 1075–1079, Mar. 2019, doi: 10.1126/science.aau7114.
- [5] T. Waddell *et al.*, “Use Of Volumetric Additive Manufacturing As An In-space Manufacturing Technology,” in *Advancements in materials applications and rapid prototyping*, 72 st International Astronautical Congress (IAC), Sep. 2022. [Online]. Available: <https://calfdm.com/wp-content/uploads/2022/09/IAC-CAL-final-15Sep22-print1.pdf>
- [6] R. Salajeghe, C. S. Kruse, D. H. Meile, D. Marla, and J. Spangenberg, “Investigating the influence of thermal and mechanical properties of resin on the sedimentation rate of the printed geometry in the volumetric additive manufacturing technique,” 2022. doi: 10.26153/tsw/44203.
- [7] R. Salajeghe, D. H. Meile, C. S. Kruse, D. Marla, and J. Spangenberg, “Numerical modeling of part sedimentation during volumetric additive manufacturing,” *Addit. Manuf.*, vol. 66, p. 103459, Mar. 2023, doi: 10.1016/j.addma.2023.103459.
- [8] H. Wang, D. J. Kline, and M. R. Zachariah, “In-operando high-speed microscopy and thermometry of reaction propagation and sintering in a nanocomposite,” *Nat. Commun.*, vol. 10, no. 1, Art. no. 1, Jul. 2019, doi: 10.1038/s41467-019-10843-4.
- [9] C. Chung Li, J. Toombs, and H. Taylor, “Tomographic color Schlieren refractive index mapping for computed axial lithography,” in *Symposium on Computational Fabrication*, Virtual Event USA: ACM, Nov. 2020, pp. 1–7. doi: 10.1145/3424630.3425421.
- [10] C. C. Li *et al.*, “Computational optimization and the role of optical metrology in tomographic additive manufacturing,” in *Advanced Fabrication Technologies for Micro/Nano Optics and Photonics XV*, SPIE, Mar. 2022, pp. 38–44. doi: 10.1117/12.2610558.

- [11] A. Orth *et al.*, “On-the-fly 3D metrology of volumetric additive manufacturing,” *Addit. Manuf.*, vol. 56, p. 102869, Aug. 2022, doi: 10.1016/j.addma.2022.102869.
- [12] A. Orth *et al.*, “Optical Scattering Tomography for Volumetric Additive Manufacturing,” in *Conference on Lasers and Electro-Optics (2022), paper ATh1D.3*, Optica Publishing Group, May 2022, p. ATh1D.3. doi: 10.1364/CLEO\_AT.2022.ATh1D.3.
- [13] J. Zhou, B. del Rosal, D. Jaque, S. Uchiyama, and D. Jin, “Advances and challenges for fluorescence nanothermometry,” *Nat. Methods*, vol. 17, no. 10, Art. no. 10, Oct. 2020, doi: 10.1038/s41592-020-0957-y.
- [14] R. Mercadé-Prieto, L. Rodríguez-Rivera, and X. D. Chen, “Fluorescence lifetime of Rhodamine B in aqueous solutions of polysaccharides and proteins as a function of viscosity and temperature,” *Photochem. Photobiol. Sci.*, vol. 16, no. 11, pp. 1727–1734, Nov. 2017, doi: 10.1039/c7pp00330g.
- [15] M. A. Bennet, P. R. Richardson, J. Arlt, A. McCarthy, G. S. Buller, and A. C. Jones, “Optically trapped microsensors for microfluidic temperature measurement by fluorescence lifetime imaging microscopy,” *Lab. Chip*, vol. 11, no. 22, pp. 3821–3828, Oct. 2011, doi: 10.1039/C1LC20391F.
- [16] P. Lavieille, F. Lemoine, G. Lavergne, and M. Lebouché, “Evaporating and combusting droplet temperature measurements using two-color laser-induced fluorescence,” *Exp. Fluids*, vol. 31, no. 1, pp. 45–55, Jul. 2001, doi: 10.1007/s003480000257.
- [17] C. M. Rackson *et al.*, “Object-space optimization of tomographic reconstructions for additive manufacturing,” *Addit. Manuf.*, vol. 48, p. 102367, Dec. 2021, doi: 10.1016/j.addma.2021.102367.
- [18] F. L. Arbeloa, P. R. Ojeda, and I. L. Arbeloa, “FLUORESCENCE SELF-QUENCHING OF THE MOLECULAR FORMS OF RHODAMINE B IN AQUEOUS AND ETHANOLIC SOLUTIONS”.
- [19] A. Vyšniauskas and M. K. Kuimova, “A twisted tale: measuring viscosity and temperature of microenvironments using molecular rotors,” *Int. Rev. Phys. Chem.*, vol. 37, no. 2, pp. 259–285, Apr. 2018, doi: 10.1080/0144235X.2018.1510461.
- [20] K. G. Casey and E. L. Quitevis, “Effect of solvent polarity on nonradiative processes in xanthene dyes: Rhodamine B in normal alcohols,” *J. Phys. Chem.*, vol. 92, no. 23, pp. 6590–6594, Nov. 1988, doi: 10.1021/j100334a023.
- [21] C. M. Rackson *et al.*, “Latent image volumetric additive manufacturing,” *Opt. Lett.*, vol. 47, no. 5, pp. 1279–1282, Mar. 2022, doi: 10.1364/OL.449220.
- [22] C. M. Rackson, “Fundamental Developments in Volumetric Additive Manufacturing,” Ph.D., University of Colorado at Boulder, United States -- Colorado, 2022. Accessed: Jun. 24, 2023. [Online]. Available: <https://www.proquest.com/docview/2671944553/abstract/7D2531D42BFC444FPQ/1>
- [23] W. Van Aarle *et al.*, “Fast and flexible X-ray tomography using the ASTRA toolbox,” *Opt. Express*, vol. 24, no. 22, p. 25129, Oct. 2016, doi: 10.1364/OE.24.025129.

## Supplementary Materials

### *S.1 Electronic synchronization of patterning projection and image acquisition*

To prevent imaging the fluorescence excited by the patterning light, the patterning and image acquisition were electronically synchronized to take place alternately. The LED of the projector was pulsed at 60 Hz at a duty cycle of 33 %. The camera was triggered immediately when this LED transition to off state and starts a 9 ms of exposure. The exposure time was chosen such that the patterning and imaging do not overlap in time.

While this approach effectively rejects fluorescence excited by the patterning light, it poses a tradeoff between time spent in patterning and in image acquisition. The maximum intensity of the patterning projections was reduced to an average of 8 mW/cm<sup>2</sup> at 33 % duty cycle from 24 mW/cm<sup>2</sup> at 100 % duty cycle. The short exposure of the camera also reduced the SNR of the acquired images.

While the camera was triggered at 60 Hz, the frames were sampled at 30 Hz in experiments such that the camera capture exactly 360 images per vial rotation for reconstruction. In future experiments, a temporal averaging technique may be applied over images collected at 60 Hz to improve SNR. The SNR could also be improved by using a stronger excitation light source and higher concentration of RhB.

### *S.2 Data acquisition, processing, and tomographic reconstruction pipeline*

All hardware control, data acquisition and processing were handled by a custom Python program. Using the multi-processing module, the main Python process spawns a new process for each of the tasks which includes image acquisition, image pre-processing, tomographic reconstruction, and data saving. This architecture was designed to concurrently process a real-time stream of data.

The image pre-processing steps included denoising, background subtraction and Ram-Lak filtering. All collected images were first Gaussian-filtered with a kernel size of 11 pixels and a standard deviation of 7 pixels for denoising. Prior to printing, a set of denoised background images was collected without the presence of excitation or patterning light while the vial was rotating. All subsequent images used for reconstruction had the background image at the corresponding angle subtracted. For the subsequent filtered backprojection step in tomographic reconstruction, the images were filtered in the horizontal direction (perpendicular to the rotation axis) by a Ram-Lak filter before they were sent to another process downstream.

The tomographic reconstruction process was performed by filtered backprojection with the Astra toolbox [23]. There are multiple methods to group images together for tomographic reconstruction. These methods are defined as time segmentation schemes in CST [9], [10]. Under the same definition, the reconstructions in this work used images within a moving window spanning one full rotation. In the real-time computation of reconstruction in this work, the entire image set was collected prior to the time of reconstruction. The reconstruction timestamps were set to be equal to the time when the last image in the set was taken. This contrasts with an offline implementation where reconstruction can be centered in the moving window.

The native tomographic reconstructions were expressed in units of greyscale value of the camera. To obtain the reconstructions in relative intensity, all reconstructions are normalized by a reference reconstruction. This reconstruction was collected one rotation prior to the start of the printing at reference temperature and  $0 \text{ mJ/cm}^3$  absorbed dose with excitation light turned on. Normalization was performed elementwise in each reconstruction voxel. After normalization, the reconstructions are expressed in  $I_{relative}$  which physically represents the ratio of fluorescence intensity relative to the same voxel at the reference state. The local  $I_{relative}$  can then be interpreted with the response surface of RhB.

### *S.3 Scattering observation by dark field imaging*

The scattering observation was done with a method similar to that of Orth *et al.* [11]. A diffused 635 nm laser source (Thorlabs CPS635S) illuminated top-down into the printing vial in the CAL system. The scattered red light entered a camera (Panasonic Lumix GH4) viewing orthogonally to the light source. A long-pass filter (FELH0600) was placed in front of the camera to remove the 405 nm patterning light from the projector. The onset of scattering was determined directly on the acquired image by the appearance of any local increase of brightness against the background at the location of the printing object. This onset happened at 42 s and 72 s for the printing of trihelix and pyramid truss target respectively.

### *S.4 Derivation of relation between spatial and fluorescence intensity resolution in tomographic imaging*

In tomographic fluorescence imaging, the value of each pixel in an image can be expressed as the line integral of fluorescence power along the line of imaging (optical axis). This approximation is accurate at the paraxial limit (when system has low NA). From this relationship, it can be shown that the resolution of fluorescence power density and spatial resolution of the tomographic reconstruction shares the total bit-depth of the camera. A high-bit-depth camera is hence desirable for obtaining high spatial resolution and temperature/DOC resolution.

In a hypothetical scenario, let  $z$  be the coordinate along the optical axis of a  $4f$  imaging system with magnification  $M$ , and  $x$  and  $y$  be the coordinates in the horizontal and vertical directions respectively. The imaging target is a fluorescent object when substantial thickness along the optical axis. The camera sensor plane is conjugate to the center plane of the imaging target. We are interested in determining the minimum change of fluorescence power density change in one reconstruction voxel that the camera pixel can detect. In a parallel beam tomographic configuration, the reconstruction voxel width equals the width of one camera pixel.

Let  $i(x', y')$  be the intensity at a particular point on the sensor plane parametrized by  $x'$  and  $y'$ ,  $\alpha(x, y, z)$  be the solid angle subtend by the objective lens from a particular point  $(x, y, z)$  in space,  $p(x, y, z)$  be the local isotropic fluorescence power density of a point  $(x, y, z)$  in space in units of  $\text{mW/cm}^3$ , and  $L(x, y)$  be  $z$ -thickness of the fluorescent object at  $(x, y)$ . Assuming all light received by the objective lens is relayed to the corresponding point on the sensor, the intensity at a point on the sensor plane can be expressed as

$$i(x' = -Mx, y' = -My) = \int_{L(x,y)} \alpha(x, y, z) p(x, y, z) dz \quad (1)$$

under the imaging condition.

From this point onwards, we only focus on events at a particular z-line at  $(x, y)$  and omit the functional dependence on  $(x, y)$  for a concise derivation. Let the bit-depth of the camera be  $b$ , and  $S$  be the saturation intensity at the given sensor setting. Each intensity level of the camera pixels is separated by  $\frac{S}{2^b}$ . Let  $p_{ref}(z)$  be the fluorescence power density at the reference state.

For a change of fluorescence power density to be detectable,

$$\frac{S}{2^b} < \Delta i = \int_L \alpha(z) p(z) dz - \int_L \alpha(z) p_{ref}(z) dz \quad (2)$$

In low-NA systems and for object with limited thickness such that  $\alpha$  can be approximated as a constant,

$$\frac{S}{2^b} < \Delta i = \alpha \int_L p(z) - p_{ref}(z) dz \quad (3)$$

If the change of fluorescence power density is concentrated at  $z_0$  along optical axis within a range  $\left[ z_0 - \frac{\Delta z}{2}, z_0 + \frac{\Delta z}{2} \right]$  where  $\Delta z$  is the thickness of one reconstruction voxel or equivalently width of one camera pixel size, then  $p(z_0)$  and  $p_{ref}(z_0)$  can be represented by their local spatial average  $p_{z_0}$  and  $p_{ref,z_0}$  respectively. We can write

$$\frac{S}{2^b} < \Delta i = \alpha \int_{z_0 - \frac{\Delta z}{2}}^{z_0 + \frac{\Delta z}{2}} p(z) - p_{ref}(z) dz \approx \alpha (p_{z_0} - p_{ref,z_0}) \int_{z_0 - \frac{\Delta z}{2}}^{z_0 + \frac{\Delta z}{2}} dz = \alpha (p_{z_0} - p_{ref,z_0}) \Delta z \quad (4)$$

From equation (4), it is clear that the product of  $(p_{z_0} - p_{ref,z_0})$  and  $\Delta z$  must be greater than a constant  $\frac{S}{\alpha 2^b}$ . For a small change in fluorescence,  $\Delta z$  must be large, which means the system has a poor reconstruction resolution. On the other hand, if  $\Delta z$  is required to be small, the fluorescence change must be large to be detectable. For a fixed hardware specification, it represents a tradeoff between spatial resolution and resolution of fluorescence power. To the goal of achieving both high spatial resolution and high temperature-DOC resolution, a high-bit-depth camera (large  $b$ ) is desirable.

We can write this equation in non-dimensional form. Let  $k$  be the ratio between the sensor saturation level and the reference state intensity at this  $(x, y)$  position, then  $S = k\alpha \int_L p_{ref}(z) dz$ . We can rewrite the detection criterion to be

$$\frac{1}{2^b} < \frac{(p_{z_0} - p_{ref,z_0}) \Delta z}{k \int_L p_{ref}(z) dz} \quad (5)$$

With a uniform excitation light, typically the fluorescence power density at the reference state is spatially constant. This leads to a form in which both the fluorescence power density change and the voxel size are non-dimensionalized:

$$\frac{1}{2^b} < \frac{1}{k} \left( \frac{p_{z_0} - p_{ref}}{p_{ref}} \right) \left( \frac{\Delta z}{L} \right). \quad (6)$$

Obviously, the above equation only states the detection requirement in idealized noise-free environments. In practical situations, the minimum change in intensity change must also be significantly greater than the average noise level  $\Delta i_{noise}$ . Following a similar argument as above, we can write the signal-to-noise requirement as

$$\Delta i_{noise} \ll \Delta i = \alpha \int_L p(z) - p_{ref}(z) dz \approx \alpha (p_{z_0} - p_{ref,z_0}) \Delta z \quad (7)$$

$$SNR = \frac{\alpha (p_{z_0} - p_{ref,z_0}) \Delta z}{\Delta i_{noise}} \gg 1. \quad (8)$$

SNR can be improved by using a larger NA (larger  $\alpha$ ), an actively cooled low-noise camera, or noise-reduction settings (longer exposure time and low gain, which lead to lower  $\Delta i_{noise}$ ).

### S.5 Resin characterization

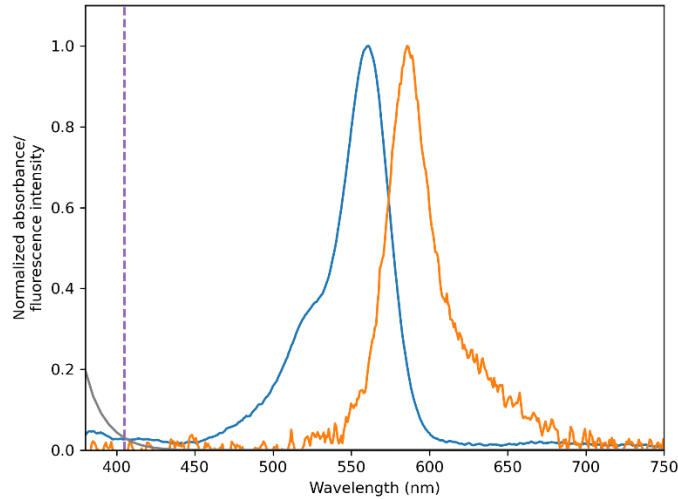


Figure S1. Normalized absorption (blue) and normalized fluorescence intensity (orange) of PEGDA-700 + 5  $\mu$ M RhB upon excitation at 532 nm, and normalized absorption of 2 mM I369 in isopropanol (gray). 405 nm patterning light used in this study is denoted in dashed line.

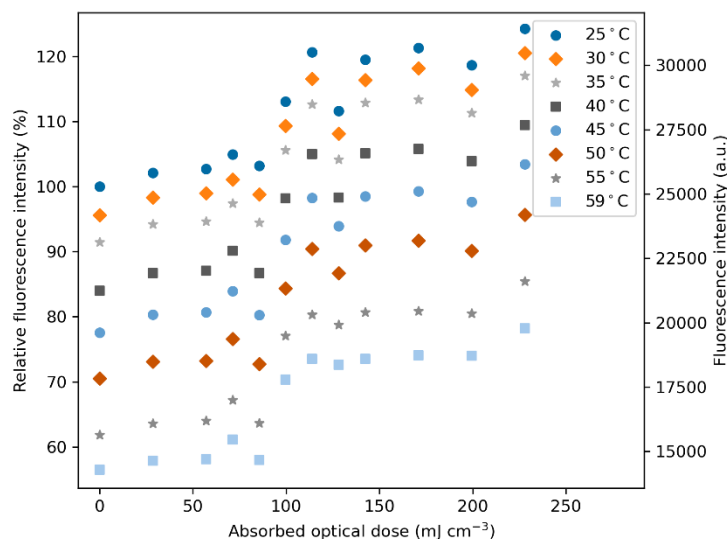


Figure S2. Fluorescence intensity (right axis) and the relative fluorescence intensity compared to a baseline of 25 °C and 0 mJ/cm<sup>3</sup> absorbed dose (left axis) of PEGDA-700 + 5 μM RhB + 0.3 mM BAPO, as a function of temperature and absorbed optical dose. The polymer precursor is excited at 532 nm.

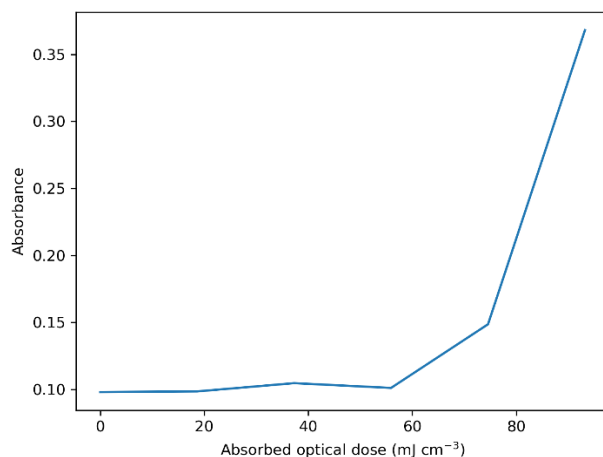


Figure S3. Absorbance of PETRA + 5 μM RhB + 0.1 wt.% I369 of various absorbed optical dose measured on a well plate. Onset of scattering is indicated by increase in measured absorbance.

### S.6. Fourier transform infrared spectroscopy measurement

The DOC (acrylate C=C double bond conversion) as a function of absorbed dose was quantified *ex situ* using Fourier transform infrared (FTIR, Bruker Vertex80) spectroscopy. Samples of thickness ~1 mm between glass slides were prepared and the instrument backgrounded to blank slides. Samples were exposed to 405 nm light (Excelitas Omnicure S2000 with a Thorlabs FBH405-10 405 nm bandpass filter) for the duration of the experiment. The intensity of the light was measured before each experiment using a handheld radiometer (Thorlabs PM100D with S121C detector). During exposure, RT-FTIR scans were done in the range of 4000 – 8000 cm<sup>-1</sup> with 4 cm<sup>-1</sup> at a frequency of 40 kHz and measurement averaging of

64 with the CaF<sub>2</sub> beamsplitter and LN-MCT Mid IR detector from Bruker. The conversion was calculated from double bond concentrations determined by integrating the 6160 cm<sup>-1</sup> C=C stretch peak using tangent skim method.

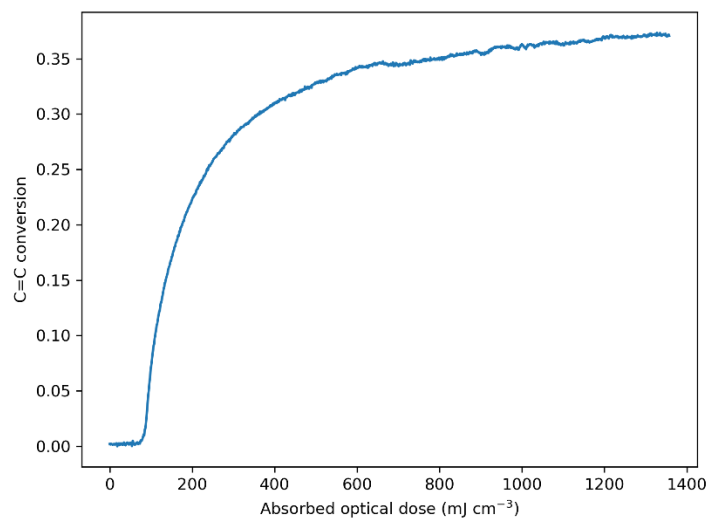


Figure S4. Real-time FTIR data of acrylate group conversion of PETRA + 5  $\mu$ M RhB + 0.1 wt. % I369.